

Training deep cross-modality conversion models with a small amount of data and its application to MVCT to kVCT conversion

Sho Ozaki,^{1,*} Shizuo Kaji,² Kanabu Nawa,³ Toshikazu Imae,³

Atsushi Aoki,³ Takahiro Nakamoto,^{3,4} Takeshi Ohta,³ Yuki Nozawa,³

Hideomi Yamashita,³ Akihiro Haga,⁵ and Keiichi Nakagawa¹

¹*Graduate School of Medicine, University of Tokyo, Tokyo 113-8655, Japan*

²*Institute of Mathematics for Industry, Kyushu University,
744 Motooka, Nishi-ku, Fukuoka 819-0395, Japan*

³*Department of Radiology, University of Tokyo Hospital, Tokyo 113-8655, Japan*

⁴*Department of Biological Science and Engineering,
Faculty of Health Sciences, Hokkaido University,
N12-W5, Kita-ku, Sapporo, Hokkaido, 060-0812, Japan*

⁵*Graduate School of Biomedical Science,
Tokushima University, Tokushima 770-8503, Japan*

Abstract

Purpose: Deep-learning-based image processing has emerged as a valuable tool in recent years owing to its high performance. However, the quality of deep-learning-based methods relies heavily on the amount of training data, and the cost of acquiring a large amount of data is often prohibitive in medical fields. Therefore, we performed CT modality conversion based on deep learning requiring only a small number of unsupervised images.

Methods: The proposed method is based on generative adversarial networks (GANs) with several extensions tailored for CT images. This method emphasizes the preservation of the structure in the processed images and reduction in the amount of training data. This method was applied to realize the conversion of mega-voltage computed tomography (MVCT) to kilo-voltage computed tomography (kVCT) images. Training was performed using several datasets acquired from patients with head and neck cancer. The size of the datasets ranged from 16 slices (for two patients) to 2745 slices (for 137 patients) of MVCT and 2824 slices of kVCT for 98 patients.

Results: The quality of the processed MVCT images was considerably enhanced, and the structural changes in the images were minimized. With an increase in the size of training data, the image quality exhibited a satisfactory convergence from a few hundred slices. In addition to statistical and visual evaluations, these results were clinically evaluated by medical doctors in terms of the accuracy of contouring.

Conclusion: We developed an MVCT to kVCT conversion model based on deep learning, which can be trained using a few hundred unpaired images. The stability of the model against the change in the data size was demonstrated. This research promotes the reliable use of deep learning in clinical medicine by partially answering the commonly asked questions: “Is our data enough? How much data must we prepare?”

* E-mail: shoozaki0117@gmail.com

I. INTRODUCTION

In recent years, cross-modality conversion associated with different imaging modalities has gained considerable attention in the radiotherapy (RT) domain [1–3]. Specifically, magnetic resonance imaging (MRI) to computed tomography (CT) conversion has been widely investigated in the context of MRI-based and MRI-guided RT [4, 5]. Cone-beam CT (CBCT) to CT conversion has been considered to enhance the image quality of CBCT, and thus, the accuracy of image-guided radiotherapy (IGRT) [6], and to facilitate its application to adaptive radiotherapy (ART) [7, 8]. Recently, certain researchers [9] investigated mega-voltage CT (MVCT) to kilo-voltage CT (kVCT) conversion to enhance the image quality of MVCT, which is considerably noisier and has a lower contrast than CBCT. Almost all practical modality conversion methods rely on deep learning (DL). In general, DL-based methods require a large amount of data for training. However, in modality conversion, many images in the corresponding modalities must be prepared, which is cumbersome for the patients and expensive for the medical staff. For instance, in the abovementioned instances of modality conversions [4–9], the training data for DL models ranged from 2795 to 6480 images. Furthermore, a question often arises regarding the number of images necessary to ensure successful training.

Notably, MVCT is used in helical tomotherapy, which is an innovative technique to administer intensity-modulated radiotherapy (IMRT) for IGRT [12–15]. To ensure precise registration based on image guidance, the image quality of the MVCT must be ensured. In addition, the MVCT images acquired in the image registration before treatment can be used for ART and dose estimation of the target and organs at risk (OAR) at intermediate fractions in the treatment. However, the images of MVCT are considerably noisier than those of kVCT. Furthermore, it is relatively difficult for MVCT to detect the soft-tissue contrast compared to the kVCT. These aspects limit the accuracy of IGRT and ART as well as the intermediate dose estimation. Certain authors [11] investigated high-dose MVCT and enhanced the image quality of MVCT. However, increasing the dose inevitably leads to an increase in the patient’s exposure. A notable advantage of the conversion approach is that it can enhance the input image quality without any increase in the dose. An alternative approach to enhance the CT image quality at the same dose is to adopt reconstruction algorithms. Iterative reconstruction with total variation regularization can suppress the

noise, although a considerable time is required to implement iterations. Nevertheless, the reconstruction speed is of significance for clinical use. Consequently, a GPU-based iterative reconstruction scheme for MVCT was developed [16], which required only a few seconds per slice without compromising the image quality. However, the image quality was not comparable to that of kVCT images, especially in terms of the noise and soft-tissue contrast detectability.

Considering these aspects, in this study, we developed a novel modality conversion model based on generative adversarial networks (GANs) [10] with several extensions, which is expected to demonstrate a high performance even when a small amount of training data is used. The design was aimed at preserving the structure in the processed images. The proposed model was applied to MVCT to kVCT conversion, and its performance was evaluated. Furthermore, we conducted a clinical evaluation in which medical doctors contoured a specific soft tissue in the processed MVCT and original MVCT images and estimated the Dice coefficient. The findings can partially address the questions regarding the adequate number of training images in deep learning, which can facilitate the reliable use of deep learning in clinical medicine.

The remaining paper is organized as follows. Section II describes the construction of the proposed model for modality conversion as well as the evaluation methods. Section III presents the results of the visual comparison among MVCT, reference kVCT, and processed MVCT images and quantitative evaluations. The dependence of the image quality and structure preservation in the processed images on the size of the training data is emphasized. Moreover, we describe the clinical evaluation of the soft tissue contouring in processed MVCT images. Section IV discusses the convergence of the image quality and limitations of the proposed approach. Section V presents the concluding remarks.

II. MATERIALS AND METHODS

A. Data acquisition

We used the MVCT and kVCT images of patients with head and neck cancer, who underwent IMRT via tomotherapy. The MVCT images pertaining to tomotherapy scans were obtained using a helical fan-beam CT scanner with a tube voltage of 3.5 MV, matrix

size of 512×512 on the axial plane with a pixel size of $0.7462 \text{ mm} \times 0.7462 \text{ mm}$, and slice thickness of 3 mm. The kVCT images were obtained using a 16-row multidetector helical CT scanner with a tube voltage of 120 kV, gantry rotation time of 0.5 s, matrix size of 512×512 on the axial plane with a pixel size of $1.074 \text{ mm} \times 1.074 \text{ mm}$, and slice thickness of 2 mm. The MVCT and kVCT images were reconstructed through filtered back-projection (FBP). The kVCT images used as Planning CT (PlanCT) and MVCT images for the image guidance were acquired on different days for each patient. Therefore, the kVCT images were not aligned to the MVCT images. Because the pixel size of the kVCT images was different from that of the MVCT images, we resized the kVCT images to a pixel size of $0.7462 \text{ mm} \times 0.7462 \text{ mm}$, similar to that of the MVCT images.

We acquired 2745 slices of MVCT from 137 patients and 2824 slices of kVCT from 98 patients as the training data. Moreover, we prepared an independent dataset consisting of 339 MVCT and 488 kVCT images from a different group of 16 patients for validation.

B. MVCT to kVCT conversion with extended GANs

x and y denote an image slice in MVCT and kVCT, respectively, represented by arrays of dimension 512×512 .

The proposed model uses x as the input and outputs a processed image slice that resembles a kVCT image. The proposed model is based on GANs and consists of three types of neural networks. To obtain a general idea of GAN-based image conversion, the reader may refer to an existing survey article [6]. An *encoder* is a network that inputs an image and outputs a latent vector that is an abstract and high-level representation of the input image. An encoder consists of down convolution layers and residual bottle-neck layers. A *decoder* is a network that inputs a latent vector and produces an image. This module consists of residual bottle-neck layers and up-sampling layers. The proposed model includes two encoders and two decoders. Certain combined networks (generators) are formulated as follows:

$$G_{\text{MV} \rightarrow \text{kV}}(x) = \text{Dec}_{\text{latent} \rightarrow \text{kV}}(\text{Enc}_{\text{MV} \rightarrow \text{latent}}(x)), \quad (1)$$

$$G_{\text{kV} \rightarrow \text{MV}}(y) = \text{Dec}_{\text{latent} \rightarrow \text{MV}}(\text{Enc}_{\text{kV} \rightarrow \text{latent}}(y)), \quad (2)$$

$$G_{\text{MV} \rightarrow \text{MV}}(x) = \text{Dec}_{\text{latent} \rightarrow \text{MV}}(\text{Enc}_{\text{MV} \rightarrow \text{latent}}(x)), \quad (3)$$

$$G_{\text{kV} \rightarrow \text{kV}}(y) = \text{Dec}_{\text{latent} \rightarrow \text{kV}}(\text{Enc}_{\text{kV} \rightarrow \text{latent}}(y)). \quad (4)$$

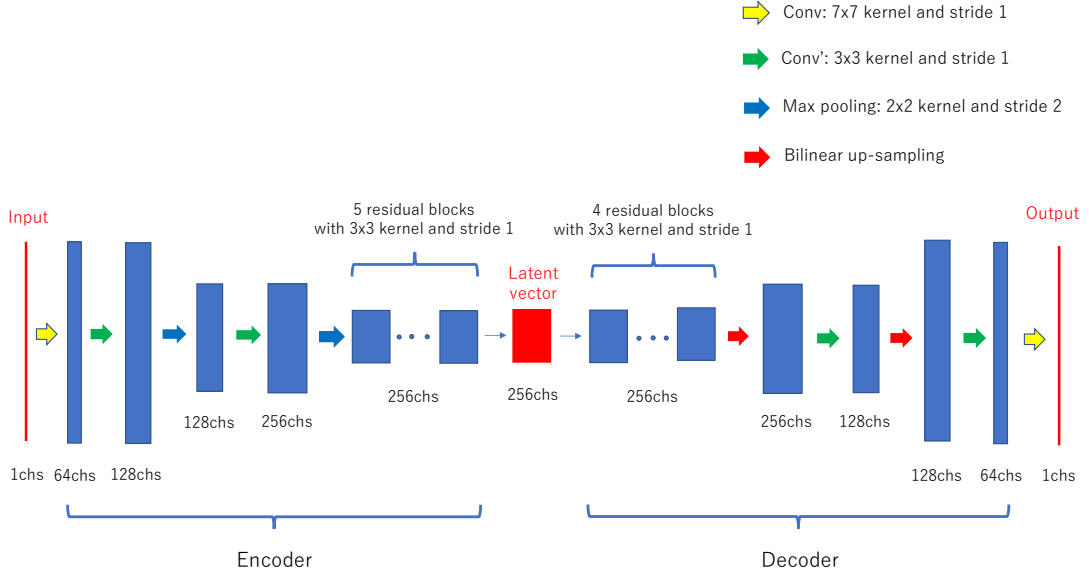


FIG. 1. Network of generators: $G_{MV \rightarrow kV}$, $G_{kV \rightarrow MV}$, $G_{MV \rightarrow MV}$, $G_{kV \rightarrow kV}$.

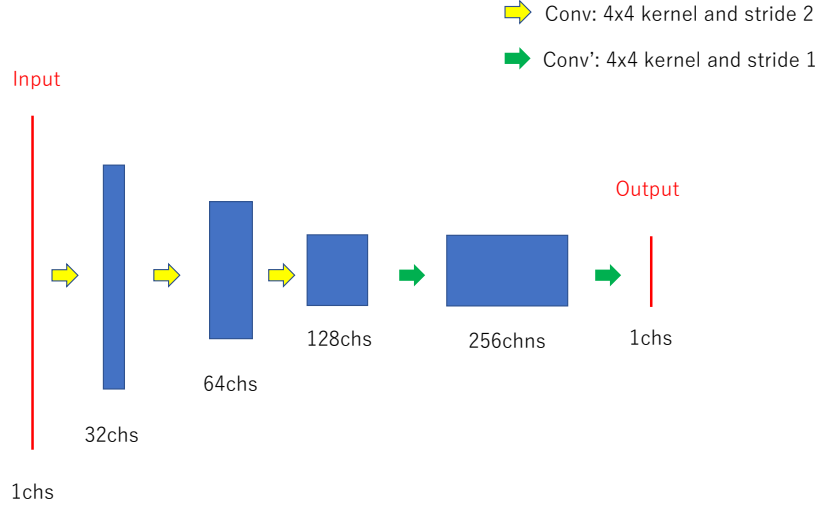


FIG. 2. Network of discriminators: D_{kV} , D_{MV} .

where Enc and Dec denote encoder and decoder, respectively, and “latent” indicates the latent vector space. Figure 1 shows the details of the generators used in this study.

A *discriminator* is a network that inputs an image and classifies it into two categories: processed and real. In this study, a typical classification network is adopted as the discriminator (Fig. 2). This network learns to output a vector consisting of 0 (processed) or 1 (real) for each image patch in the input image. We adopt two discriminators: D_{kV} aims to distinguish the real kVCT images from the processed MVCT (kVCT-like) images, and D_{MV}

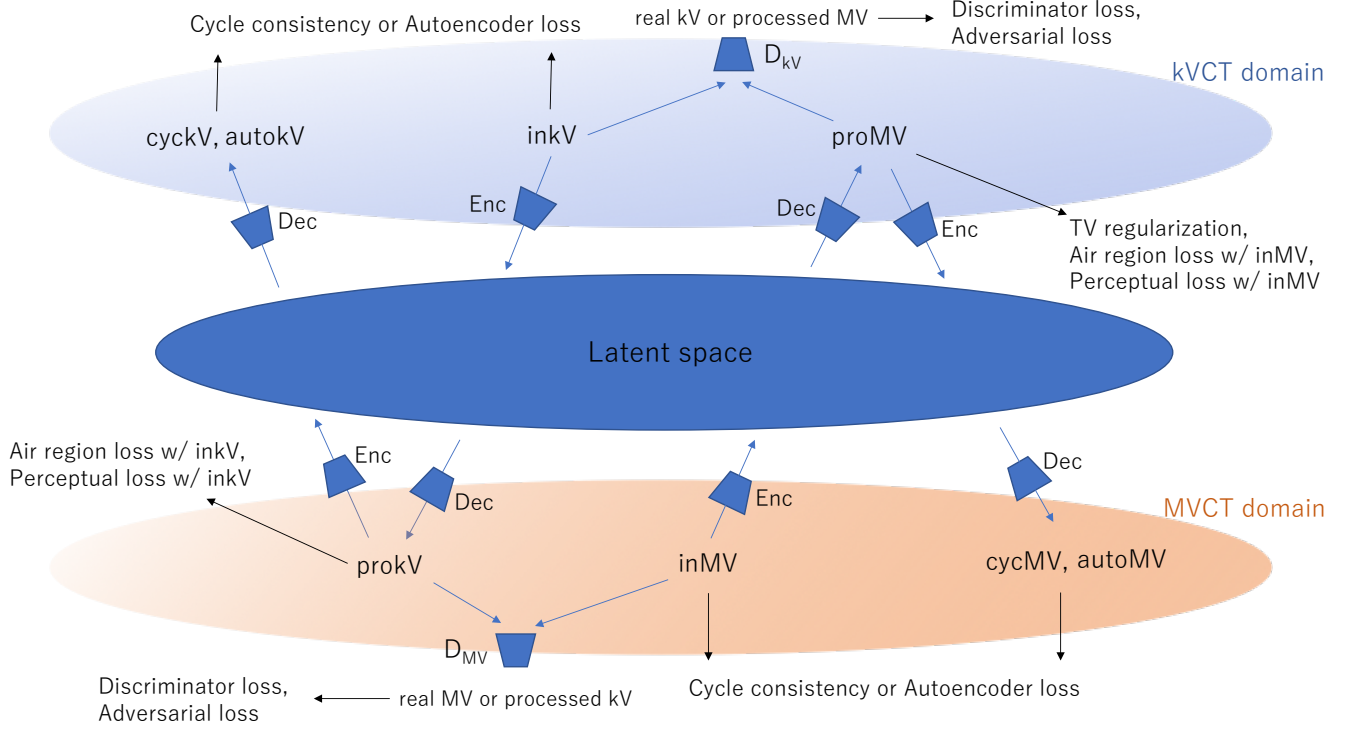


FIG. 3. Schema of our networks with loss functions.

aims to distinguish the real MVCT images from the processed kVCT (MVCT-like) images. These discriminators learn the distribution of the real kVCT (MVCT) images and help the encoders and decoders produce images according to the distribution.

The ideal output of D_{kV} is all zero or one elements for a processed MVCT image or real kVCT image, respectively:

$$D_{kV}(v) \rightarrow \begin{cases} 0 & (\text{if } v \text{ is processed MVCT image.}) \\ 1 & (\text{if } v \text{ is kVCT image.}) \end{cases} \quad (5)$$

Similarly, the ideal output of D_{MV} is

$$D_{MV}(v) \rightarrow \begin{cases} 0 & (\text{if } v \text{ is processed kVCT image.}) \\ 1 & (\text{if } v \text{ is MVCT image.}) \end{cases} \quad (6)$$

We define the loss function \mathcal{L}_D for the discriminators by considering the squared distance

from the ideal output:

$$\mathcal{L}_D = \lambda_D \left\{ \sum_{x \in \mathbf{MV}} (\|D_{\mathbf{kV}}(G_{\mathbf{MV} \rightarrow \mathbf{kV}}(x)) - \mathbf{0}\|^2 + \|D_{\mathbf{MV}}(x) - \mathbf{1}\|^2) + \sum_{y \in \mathbf{kV}} (\|D_{\mathbf{MV}}(G_{\mathbf{kV} \rightarrow \mathbf{MV}}(y)) - \mathbf{0}\|^2 + \|D_{\mathbf{kV}}(y) - \mathbf{1}\|^2) \right\}, \quad (7)$$

where \mathbf{MV} and \mathbf{kV} are the sets of training MVCT and kVCT images, respectively.

The loss function \mathcal{L}_G for the encoders and decoders consists of several terms:

$$\mathcal{L}_G = \lambda_{\text{cycle}} \mathcal{L}_{\text{cycle}} + \lambda_{\text{autoenc}} \mathcal{L}_{\text{autoenc}} + \lambda_{\text{adv}} \mathcal{L}_{\text{adv}} + \lambda_{\text{tv}} \mathcal{L}_{\text{tv}} + \lambda_{\text{air}} \mathcal{L}_{\text{air}} + \lambda_{\text{percep}} \mathcal{L}_{\text{percep}}, \quad (8)$$

where $\mathcal{L}_{\text{cycle}}$ is the cycle consistency loss, $\mathcal{L}_{\text{autoenc}}$ is the autoencoder loss, \mathcal{L}_{adv} is the adversarial loss, \mathcal{L}_{tv} is the total variation regularization, \mathcal{L}_{air} is the air-region loss, $\mathcal{L}_{\text{percep}}$ and is the perceptual loss. Although $\mathcal{L}_{\text{cycle}}$, \mathcal{L}_{adv} , and \mathcal{L}_{tv} are standard in CycleGAN-based models and their variants, the remaining terms are tailored for CT image conversion.

The cycle consistency loss [17] is defined using the L^1 -norm:

$$\mathcal{L}_{\text{cycle}} = \sum_{x \in \mathbf{MV}} \|x - G_{\mathbf{kV} \rightarrow \mathbf{MV}}(G_{\mathbf{MV} \rightarrow \mathbf{kV}}(x))\|_1 + \sum_{y \in \mathbf{kV}} \|y - G_{\mathbf{MV} \rightarrow \mathbf{kV}}(G_{\mathbf{kV} \rightarrow \mathbf{MV}}(y))\|_1, \quad (9)$$

which ensures that $G_{\mathbf{kV} \rightarrow \mathbf{MV}}$ and $G_{\mathbf{MV} \rightarrow \mathbf{kV}}$ are mutually inverse. The autoencoder loss is

$$\mathcal{L}_{\text{autoenc}} = \sum_{x \in \mathbf{MV}} \|x - G_{\mathbf{MV} \rightarrow \mathbf{MV}}(x)\|_1 + \sum_{y \in \mathbf{kV}} \|y - G_{\mathbf{kV} \rightarrow \mathbf{kV}}(y)\|_1. \quad (10)$$

The cycle consistency and autoencoder losses function as regularizers and help enhance the stability. The adversarial loss is defined as

$$\mathcal{L}_{\text{adv}} = \sum_{x \in \mathbf{MV}} \|D_{\mathbf{kV}}(G_{\mathbf{MV} \rightarrow \mathbf{kV}}(x)) - \mathbf{1}\|^2 + \sum_{y \in \mathbf{kV}} \|D_{\mathbf{MV}}(G_{\mathbf{kV} \rightarrow \mathbf{MV}}(y)) - \mathbf{1}\|^2. \quad (11)$$

This loss encourages the encoders and decoders to produce images according to the distribution of the training data learnt by the discriminators. The adversarial loss encourages the encoders and decoders to change the structures pertaining to the initial images, which leads to instability in learning GANs. Consequently, we include various losses that serve as regularizers.

The total variation regularization can be defined as

$$\mathcal{L}_{\text{tv}} = \sum_{x \in \mathbf{MV}} \|\text{grad}(G_{\mathbf{MV} \rightarrow \mathbf{kV}}(x))\|_1, \quad (12)$$

where grad is the image gradient. This framework encourages the generator to produce spatially uniform images. The air-region loss is defined as

$$\mathcal{L}_{\text{air}} = \sum_{x \in \mathbf{MV}} \|\psi(G_{\text{MV} \rightarrow \text{kV}}(x)) - \psi(x)\|_1 + \sum_{y \in \mathbf{kV}} \|\psi(G_{\text{kV} \rightarrow \text{MV}}(y)) - \psi(y)\|_1, \quad (13)$$

where

$$\psi(z) = \begin{cases} z & (\text{if } z < C), \\ 0 & (\text{if } z \geq C), \end{cases} \quad (14)$$

where C is a constant equivalent to -598 HU. This loss ensures that the generators do not alter the regions having values less than -598 HU to preserve the air-body boundaries.

The perceptual loss is defined as

$$\mathcal{L}_{\text{percep}} = \frac{1}{whn_{\text{cl}}} \left(\sum_{x \in \mathbf{MV}} \|\phi(G_{\text{MV} \rightarrow \text{kV}}(x)) - \phi(x)\|^2 + \sum_{y \in \mathbf{kV}} \|\phi(G_{\text{kV} \rightarrow \text{MV}}(y)) - \phi(y)\|^2 \right) \quad (15)$$

where ϕ is the output of the second convolutional layer of the VGG networks pre-trained by the natural images derived from the ImageNet database. w, h, n_{cl} denote the width, height, and number of channel of this layer, respectively. The second (and, in general, a shallow) layer of the VGG network is known to learn low-level image features such as edges. The perceptual loss helps to preserve the boundary of different regions in the CT image.

A schema of the proposed networks and loss functions is presented in Fig. 3. We empirically select the hyperparameters in the loss functions as follows:

$$\lambda_{\text{cycle}} = 10.0, \quad \lambda_{\text{autoenc}} = 1.0, \quad \lambda_{\text{adv}} = 0.1, \quad \lambda_{\text{tv}} = 0.001, \quad \lambda_{\text{D}} = 1.0, \quad \lambda_{\text{air}} = 1.0, \quad \lambda_{\text{percep}} = 0.1.$$

To ensure the training efficiency, the values of the CT images are clipped to $[-600, 400]$ HU and scaled to $[-1, 1]$. In other words, the pixels with an HU below -600 and above 400 are mapped to -1 and 1 , respectively. To perform data augmentation during the training, the cropped images are randomly rotated (up to 20°), translated (up to 50 pixels), and scaled (from 0.9 to 1.1) before being cropped randomly around the center to a size of 300×360 pixels. This size is selected to ensure that the head and neck are contained within the edges to avoid the boundary effect of convolutional neural networks.

In this study, the numerical experiments were conducted using a personal computer equipped with a single GPU (Nvidia 2080Ti) and a CPU (Intel Core i9-9940X) with 64 GB memory, running Ubuntu 16.04 LTS. We implemented our algorithm with Python 3.7.5

and Chainer 7.2.0. The codes used in this study are available on Github¹. The training required approximately two days. The conversion from MVCT images to processed MVCT images using the trained model required approximately a few seconds for 20 slices of one patient.

C. Evaluation methods

1. Quantitative evaluation

An independent dataset consisting of unaligned MVCT and kVCT images derived from sixteen patients with head-and-neck cancer, #1–#16, were used for the quantitative evaluations. In addition to visual inspection and the basic statistical analysis based on the histogram of HU values, we adopted the following evaluation metrics to quantify the validity of our model.

To quantitatively evaluate the degree of noise reduction in the processed MVCT (kVCT-like) images, we propose a new metric, noised SelfSSIM (NSelfSSIM), defined as

$$\text{NSelfSSIM}(img) = \text{SSIM}(img, img + \text{Gaussian noise with } \sigma = 6), \quad (16)$$

where SSIM is the structural similarity index measure. The rationale is that if the original image img has low noise, it is significantly different in terms of the SSIM when Gaussian noise is added. Accordingly, NSelfSSIM exhibits lower values if the image has a lower noise level. This metric can quantitatively indicate the noise reduction in the processed images.

To quantify the structural preservation, we introduce two other indexes, namely, the difference in gradient (DIG) and cycle consistency error (CCE). The DIG is defined as

$$\mathcal{L}_{\text{grad}}(x) = \|\text{grad}(x - G_{\text{MV} \rightarrow \text{kV}}(x))\|^2, \quad (17)$$

where x is the input MVCT image. The DIG measures the change in the pixel values of the original and processed images in the gradient domain, thereby evaluating the preservation of the edges.

The CCE is defined as

$$\mathcal{L}_{\text{cycle}}(x) = \|x - G_{\text{kV} \rightarrow \text{MV}}(G_{\text{MV} \rightarrow \text{kV}}(x))\|_1, \quad (18)$$

¹ <https://github.com/shizuo-kaji/UnpairedImageTranslation>

where x is the input MVCT image. The CCE is large if $G_{\text{MV} \rightarrow \text{kV}}(x)$ is altered irreversibly from x .

2. Clinical evaluation

The clinical relevance of the quality improvement of the processed images was considered. Specifically, five medical doctors of radiotherapy in the University of Tokyo Hospital contoured the parotid glands of three patients, considering the validation dataset including the processed MVCT, original MVCT, and PlanCT (kVCT) images. For this evaluation, we adopted the PlanCT (kVCT) images acquired on the same day as that when the MVCT images of the same patient were acquired. Moreover, 3D rigid registration from the PlanCT images to the MVCT images was conducted using 3-D Slicer [18]. We considered the average of five contours on the PlanCT images provided by the five doctors, and regarded the average contour as the ground truth. The average of the contours refers to the binarization of the average of five binary images at a threshold of 0.5. We calculated the Dice coefficients between the contours in the processed MVCT and the ground truth and those between the contours on the original MVCT and the ground truth.

III. RESULTS

To evaluate the performance of the proposed model, it was applied to realize MVCT to kVCT conversion to enhance the image quality of MVCT when using a small amount of data. As described in §II A, we used 2745 slices of MVCT from 137 patients and 2824 slices of kVCT from 98 patients for training. To assess the impact of the data size on the model performance, we prepared reduced-size datasets composed of 16, 32, 64, 128, 256, 512, 1024, and 2048 slices for each MVCT and kVCT case, labeled as data-16, data-32, data-64, data-128, data-256, data-512, data-1024, data-2048, and data-full, respectively. Data-full represents the dataset containing all the images (2745 slices of MVCT and 2824 slices of kVCT). The number of patients and slices in each dataset are summarized in TABLE I.

Furthermore, we used a dataset consisting of MVCT and kVCT images from 16 additional patients (labeled #1–#16) for validation. To avoid the metal artifact in the oral cavity region that often appears in kVCT images, we used the slices from the mandibular to the base of

TABLE I. Datasets

	data-16	data-32	data-64	data-128	data-256	data-512	data-1024	data-2048	data-full
Patients	2	4	8	16	32	64	80	120 (MVCT), 95 (kVCT)	137 (MVCT), 98 (kVCT)
Slices	16	32	64	128	256	512	1024	2048	2745(MVCT) , 2824 (kVCT)

the neck for training and validation.

Figures 4 and 5 show the visual comparison among the MVCT, processed MVCT, and kVCT images of patients #1 and #2, pertaining to several datasets. In addition, the kVCT images of the same patients are shown for reference. It must be noted that the processed MVCT image are not expected to exactly match the kVCT image because the MVCT and kVCT images were obtained on different days. Nevertheless, the kVCT image of the same patient can serve as a valuable reference for the visual comparison. The figures highlight the considerable enhancements in the image quality. Even in the case of data-16, the noise is considerably reduced, and thus, the contrast is enhanced, while preserving the structures. A similar improvement can be observed for all validation datasets #1-#16. Figure 6 shows a sample failure image produced by the model trained with only eight slices from one patient. It was difficult for the model to preserve the structures of the input images. Thus, we performed an evaluation involving different data sizes, up to 16 slices from two patients. Figure 7 shows the histograms of the images shown in Figs. 4 and 5. The histograms of the processed MVCT images were similar to those of the kVCT images. Although the histograms of the processed MVCT images did not necessarily coincide with those of the kVCT image, for the abovementioned reason, they were expected to be similar for the same patient. In the histograms of the processed MVCT images, the peaks corresponding to the muscle and fat were well separated. This finding indicates that the contrast between the muscle and fat was enhanced in the processed MVCT images. This finding is consistent with that obtained in the visual comparisons. The results of the histograms converged well with the increase in the data size.

Figure 8 shows the DIG of the images processed using the proposed model and original CycleGAN model² with data-16. In the results obtained using the proposed model, the positions of the structures are retained. In contrast, the result of the original CycleGAN involves a large deviation from the original position in the input image. The CCE values

² Only the cycle consistency loss, adversarial loss, and discriminator loss were used in training, and deconvolution was employed for up-sampling, as described in [17].

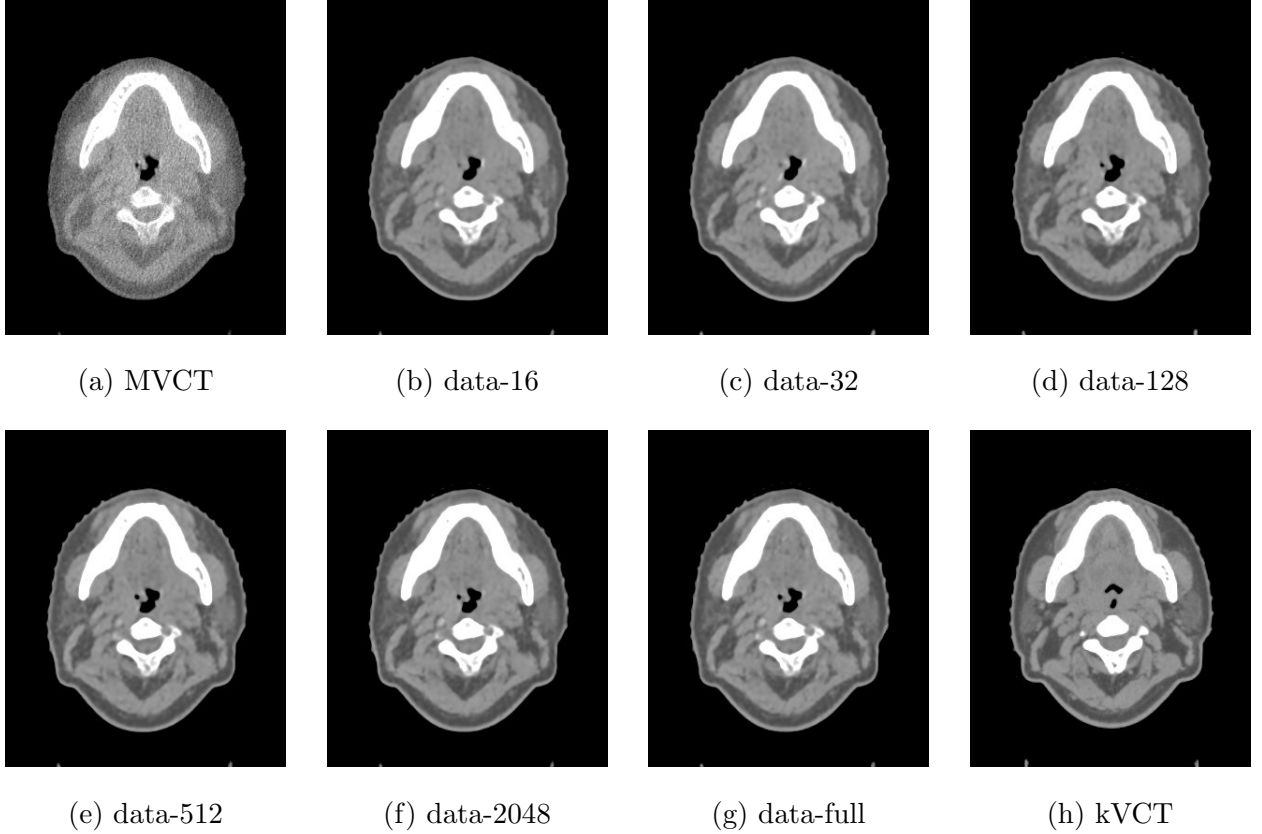


FIG. 4. Visual comparison of image quality among MVCT, processed MVCT and reference kVCT images of patient #1. For the processed MVCT, images generated from the models trained by data-16, data-32, data-128, data-512, data-2048, and data-full are shown. The display window range is set as $(-300, 300)$ HU.

are shown in Fig. 9. The original CycleGAN cannot retain the structure of the input image (right panel in Fig. 9), although the proposed model can effectively preserve the structures (left panel of Fig. 9). Figure 10 compares the box plot of the DIG pertaining to the proposed model and original CycleGAN trained with data-16. Thirty slices of validation data were used for the evaluation. The median DIG of the proposed model and CycleGAN was 0.0560 and 0.0816, respectively. This difference was statistically significant with the p-value being less than 0.001. These differences in the proposed model and original CycleGAN were more pronounced when the models were trained with a small amount of data. In general, structural changes are highly undesirable in image registration and dose calculation. Thus, when using a small amount of data for training, the proposed model outperforms the original CycleGAN in terms of the conservation performance. Figure 11 shows the data size dependence of the

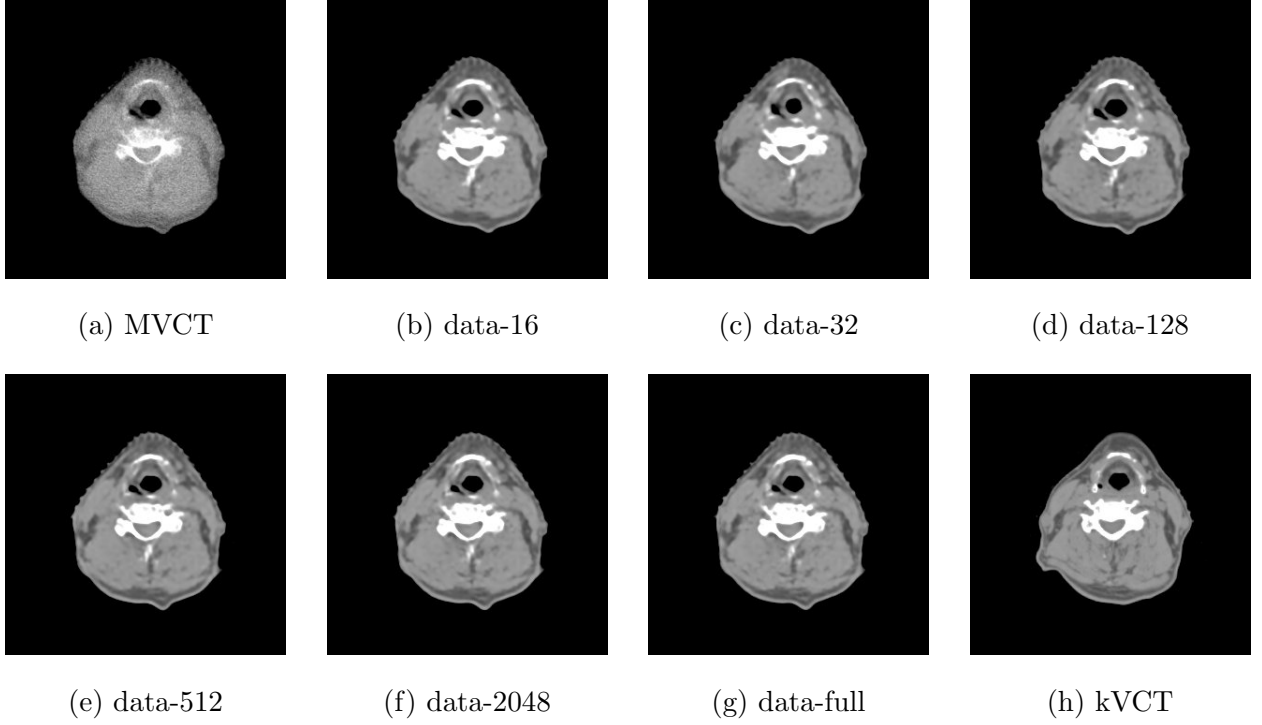


FIG. 5. Visual comparison of the quality among the MVCT, processed MVCT and reference kVCT images of patient #2. The display window range is set as (-300, 300) HU.

DIG. We used all validation slices for evaluating the DIG. In the small data region, the DIG fluctuated slightly; however, for data sizes above 256, the DIG converged with fewer fluctuations. The DIG values pertaining to data-256, data-512, data-1024, and data-2048 did not exhibit statistically significant differences from that of the data-full, within the minor shift of the value of 0.003 in the DIG.

The mean value and standard deviation (SD) of the HU of soft tissues for different datasets are listed in TABLE II. In the statistical evaluations of the HU of the muscle and fat, an ROI of 10×10 pixels was extracted from patients #1–#4 for the muscle and patients #5–#8 for the fat. For the spinal cord and tongue, we selected four slices with an interval of 2 and 3 mm for kVCT and MVCT, respectively, with the four slices extracted from patients #9–#12 for the spinal cord and patients #13–#16 for the tongue. In each slice, one square ROI sized 10×10 pixels was selected in the regions of the same soft tissue area (spinal cord or tongue). Accordingly, 16 ROIs were selected for each soft tissue to evaluate the HU. In TABLE II, the large noise of MVCT images is reflected in the large values of the SD of MVCT. In this context, small SD values for the processed MVCT compared to those

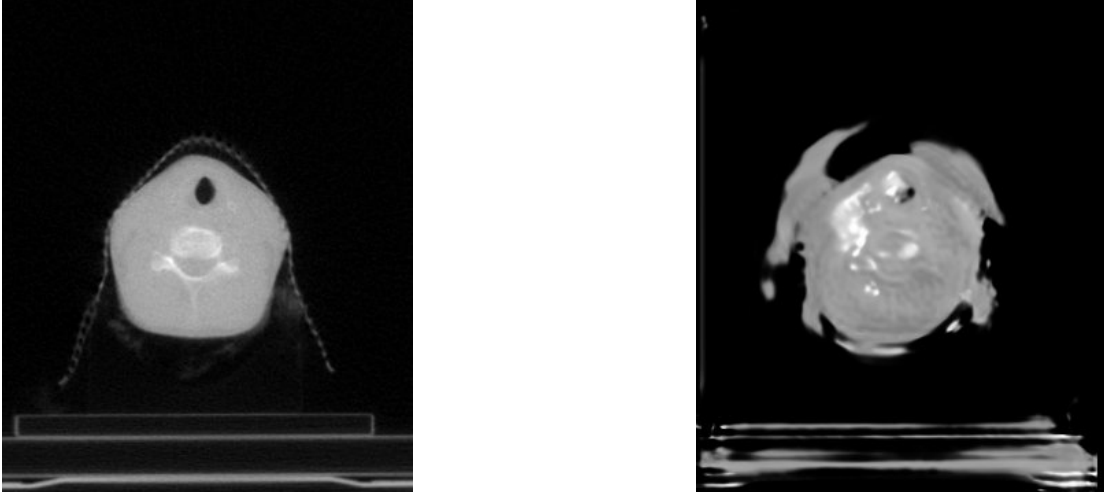


FIG. 6. Sample failure image (right panel) generated by the modal trained with only eight slices from one patient. The left panel shows the original MVCT image.

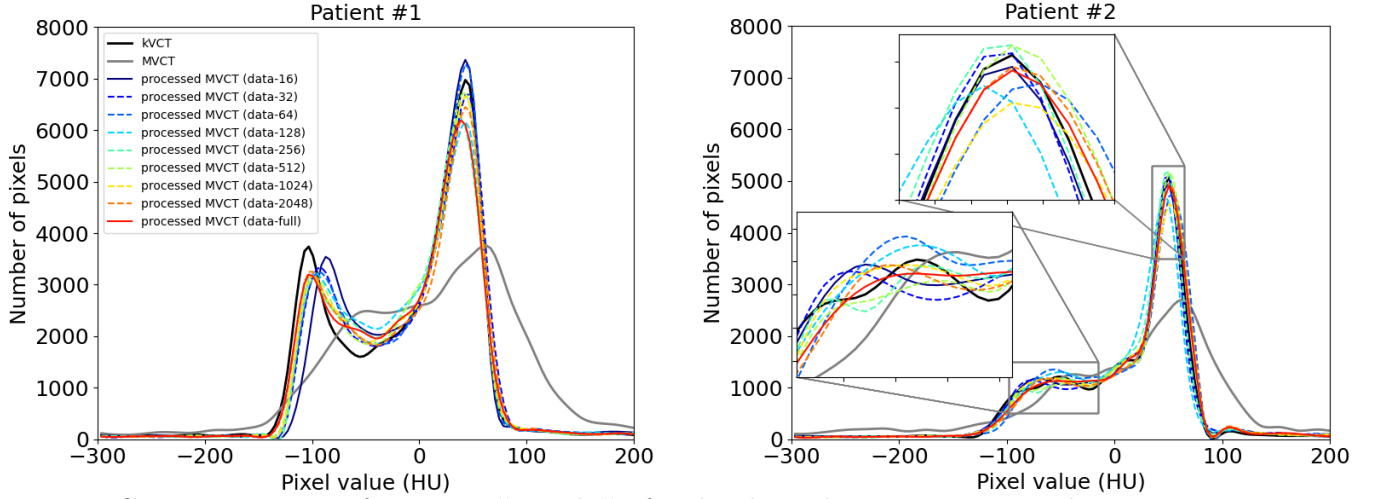


FIG. 7. Histograms of patients #1 and #2 for the slices shown in Figs. 4 and 5.

of the MVCT indicated noise reduction. The mean and SD values of the processed MVCT approached those of the kvCT as the data size increased. Figure 12 shows the soft tissue contrast defined by the HU difference between the fat and muscle. As the data size increased, the contrast slightly increased, and from data-256, the values became almost constant.

TABLE III presents the results of NSelfSSIM, defined in Eq. (16), evaluated for 30 ROIs sized 80×80 from each MVCT, processed MVCT, and kvCT. The HU values were scaled to $[0, 255]$. A lower NSelfSSIM of the processed MVCT compared to that of the MVCT quantitatively indicated a noise reduction. The values of the processed MVCT images were

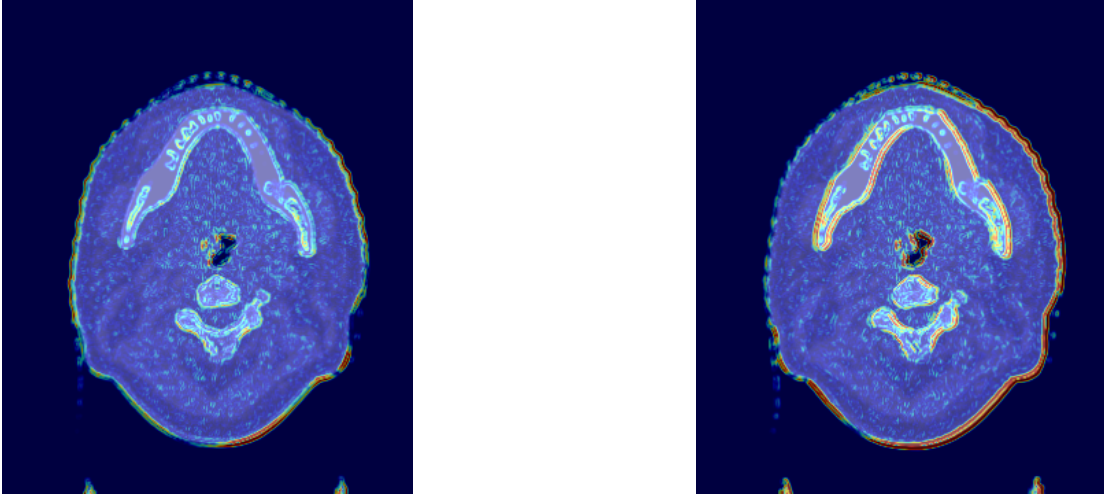


FIG. 8. Heat map comparison of the DIG of the proposed model (left panel) and original CycleGAN (right panel). A slice of patient #1 is shown.

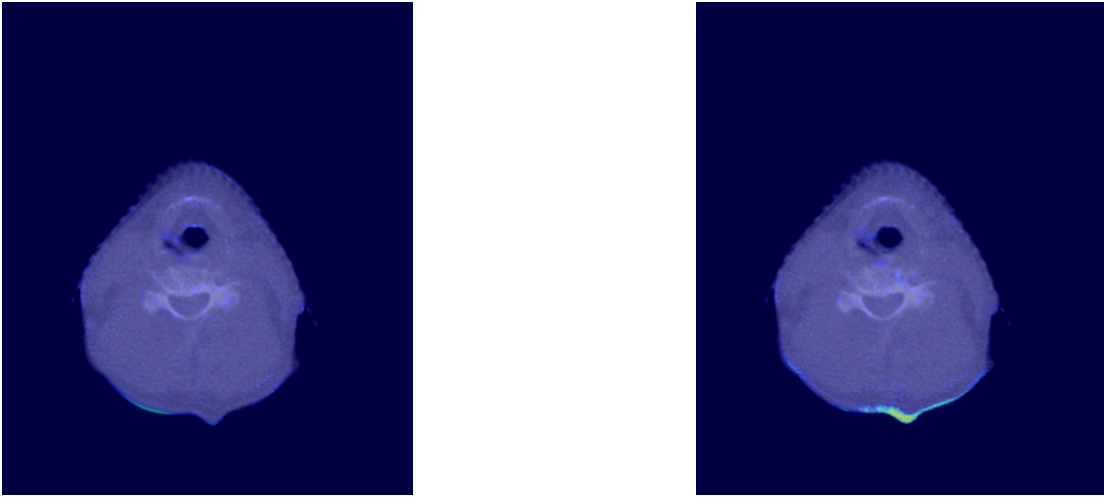


FIG. 9. Heat map comparison of the CCE between the proposed model (left panel) and original CycleGAN (right panel). A slice of patient #2 is shown.

constant against the change in the data size, and they were compatible with those of the kVCT within the standard deviation.

In terms of the clinical evaluation of the image quality, as described in Section II-C, to ensure that the registered PlanCT images are suitable as the ground truth of the clinical evaluation, Fig. 13 shows the checkerboards comparing the registered PlanCT images and MVCT images. Moreover, Fig. 14 shows the results of the Dice coefficients of the MVCT and processed MVCT from the models trained with data-16, data-256, and data-full. The

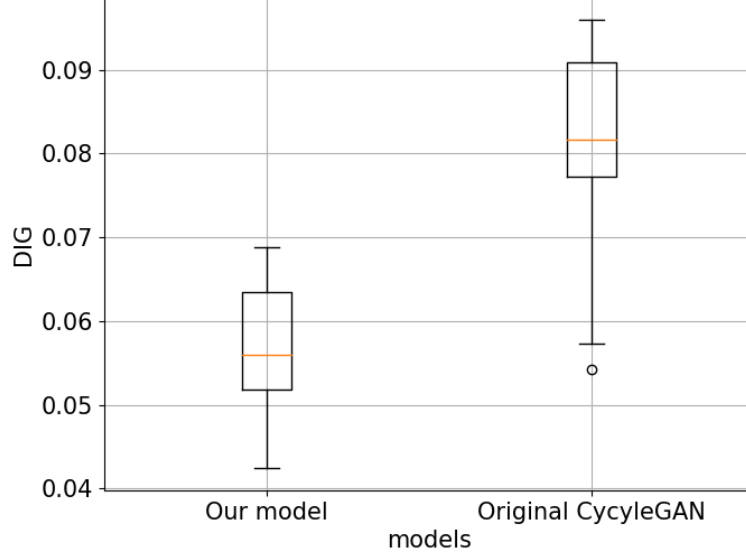


FIG. 10. Box plot comparison of the DIG for the proposed model and original CycleGAN trained with data-16.

TABLE II. Mean value and standard deviation of the soft tissues in the HU

		MVCT	data-16	data-32	data-64	data-128	data-256	data-512	data-1024	data-2048	data-full	kVCT
Fat	Mean	-79.1	-81.5	-90.3	-94.9	-95.9	-101.1	-104.6	-103.7	-103.2	-102.4	-108.3
	SD	31.1	20.7	21.3	17.1	16.9	18.0	17.0	15.5	14.0	14.8	16.9
Muscle	Mean	57.3	43.0	48.8	47.7	49.8	48.5	49.2	46.9	48.8	48.4	51.2
	SD	30.6	15.0	13.0	18.1	15.7	14.6	13.9	14.0	13.2	15.1	10.4
Spinal cord	Mean	75.2	29.1	24.5	30.9	25.3	23.9	25.0	23.2	27.9	27.5	25.0
	SD	30.1	12.9	15.8	12.1	12.9	12.9	12.8	11.5	11.5	11.2	8.8
Tongue	Mean	78.8	46.2	56.4	43.9	50.2	46.2	48.9	51.9	50.6	49.6	54.2
	SD	27.4	11.6	13.8	11.1	13.9	13.6	14.6	15.1	13.2	13.1	14.5

statistical results corresponding to Fig. 14 are presented in TABLE IV. The median values of data-256 and data-full were larger than those of MVCT, and the differences from the MVCT were statistically significant. However, a significant difference between data-16 and MVCT was not observed. Moreover, the Dice coefficient of data-256 did not exhibit a significant difference with that for the data-full case. This finding clinically supported the results obtained in the quantitative evaluation, in which the values of several indexes remained nearly constant against the change in the data size.

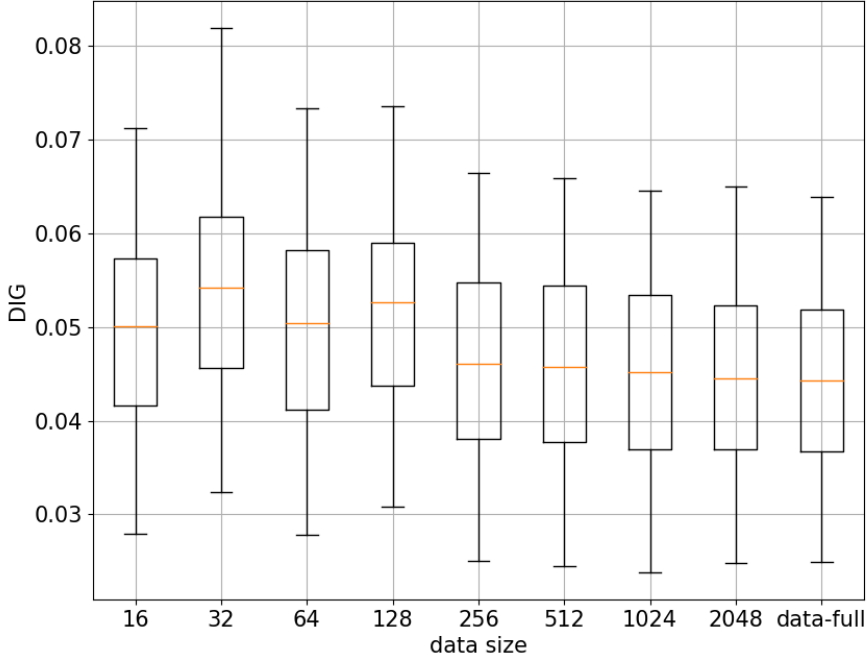


FIG. 11. Data size dependence of the DIG.

TABLE III. Mean value and standard deviation of NSelfSSIM.

	MVCT	data-16	data-32	data-64	data-128	data-256	data-512	data-1024	data-2048	data-full	kVCT
Mean	0.9024	0.6592	0.6783	0.6678	0.7004	0.6927	0.6935	0.7015	0.7004	0.7079	0.7263
SD	0.0106	0.0935	0.0807	0.0953	0.0807	0.0800	0.0822	0.0797	0.0834	0.0794	0.0825

IV. DISCUSSION

In the application of deep-learning-based approaches, questions often arise regarding the adequate amount of training data. Considering the abovementioned results, we formulated suggestions on how to decide the amount of training data in deep learning, especially in

TABLE IV. Statistics of the Dice coefficient.

	Median	P value w.r.t. MVCT	P value w.r.t. data-full
MVCT	0.656	-	-
data-16	0.640	0.68	< 0.001
data-256	0.687	< 0.001	0.73
data-full	0.693	< 0.001	-

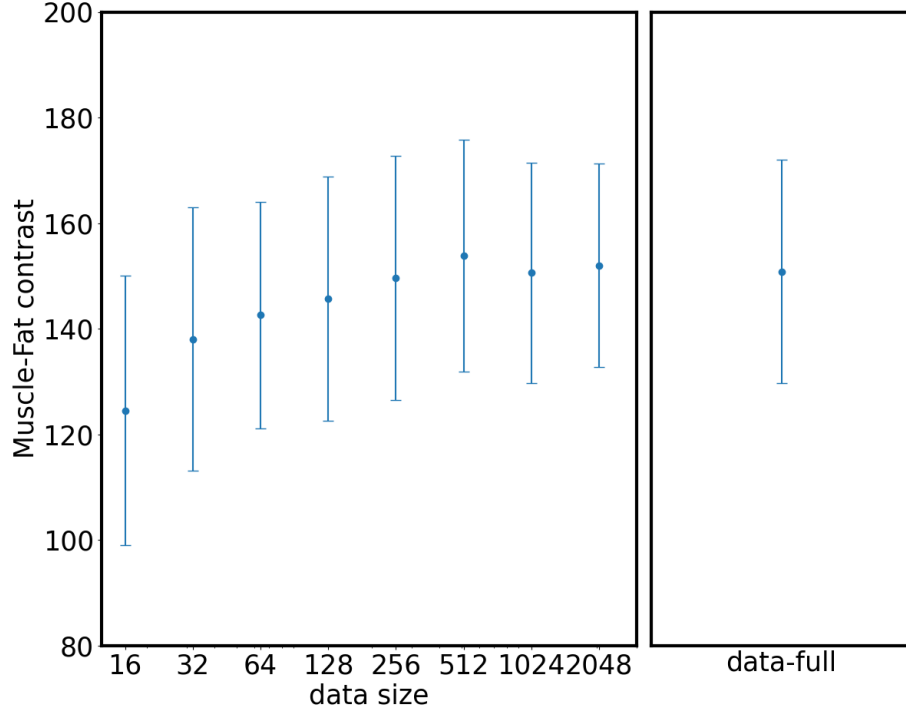


FIG. 12. Soft tissue contrast defined by the difference in the muscle and fat in HU.

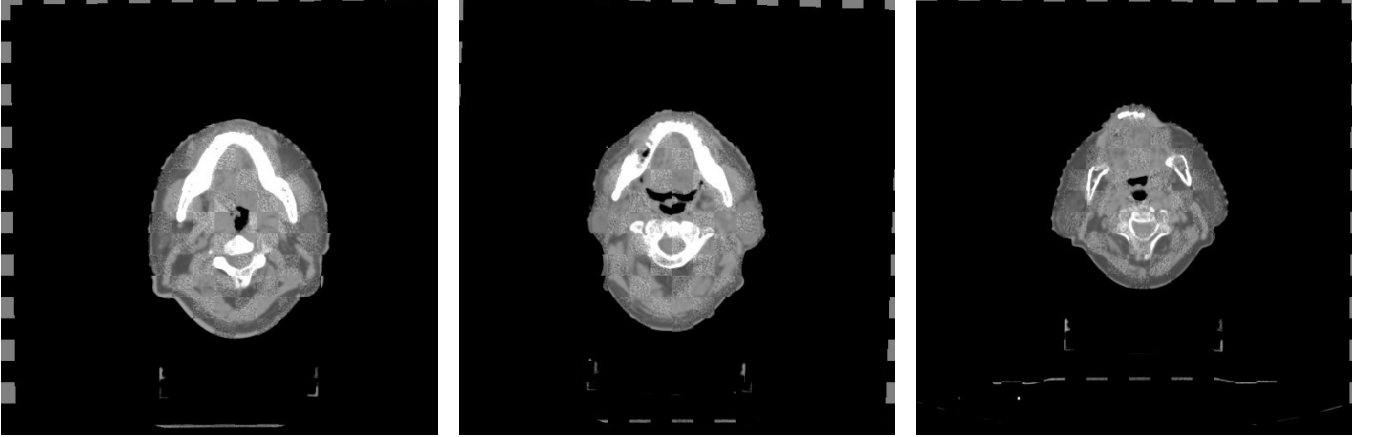


FIG. 13. Checkerboard of registered images.

medical imaging applications. In particular, we investigated the data size dependence of the obtained results and noted that several quantitative indexes, including the HU values of soft tissues, DIG, and NSelfSSIM became nearly constant for 256 images against the change in the data size. Moreover, in the clinical evaluations, we compared the accuracy of the contours on the images processed using the models trained with 256 images and full dataset (having thousands of images). The accuracies of contours on both types of processed

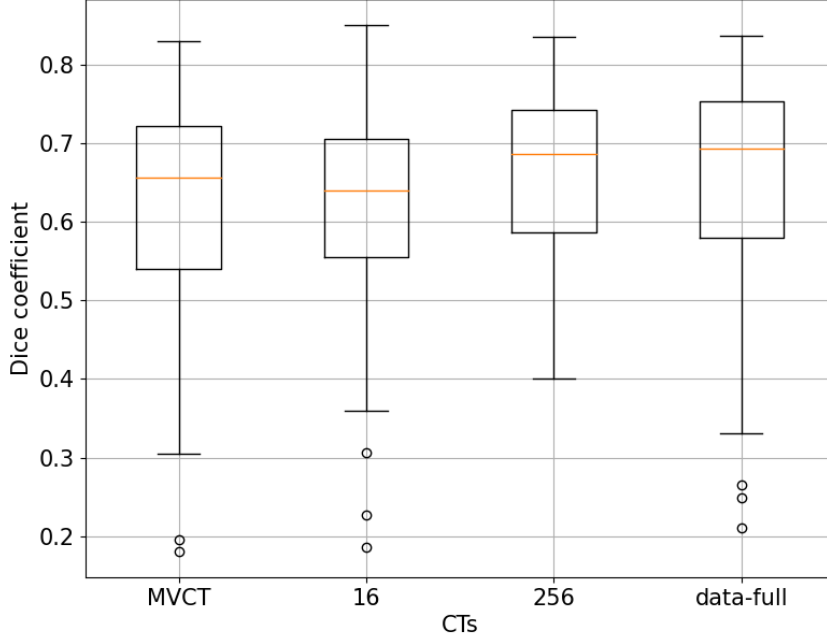


FIG. 14. Box plots of Dice coefficients. For each CT, five doctors contoured the parotid glands of three patients of validation. The Dice coefficients were evaluated using the registered PlanCT as the ground truth.

images were comparable with no statistically significant difference. The clinical result and results of the data size dependence of the quantitative indexes indicated that the image quality converged beyond 256 images. This convergence of the image quality can partly answer the question regarding the adequate amount of training data in deep learning. In this manner, we can suitably select the number of training images for deep learning-based image processing, which can promote the reliable use of deep learning in clinical medicine.

In general, deep learning approaches are believed to be data intensive, and tens to hundreds of thousands of images are typically required for natural image recognition and classification. In the field of modality conversions, certain researchers reported the use of thousands of images [4–9]. Nevertheless, the proposed model exhibits a competitive performance with a considerably smaller dataset that consists of merely 256 images. The key to achieve such a high performance with a small amount of data pertains to the newly introduced loss functions. These loss functions suitably regularize the model parameters, leading to structure preservation and stability against the reduction in the data size.

Finally, we consider the limitation pertaining to metal artifacts. In this study, we used

images from the mandibular to the base of the neck to avoid the metal artifact in the oral cavity region, which usually appears in PlanCT images. This aspect leads to a limitation in the z-direction, and it might be a bottleneck in the clinical use of our approach, such as in dose calculation. To overcome the limitation, the following three possibilities can be considered:

- Using artifact-reduced PlanCT images derived using the SEMAR algorithm [19, 20] for training
- Using artifact-free PlanCT images generated by a deep-learning-based method such as that described previously [21] for training
- Using a deep image prior [22] without PlanCT images (that is, without learning)

These aspects may be considered in future work.

V. CONCLUSION

We constructed a modality conversion model based on deep learning and applied it to realize MVCT to kVCT conversion to enhance the image quality of MVCT in helical tomotherapy. The proposed model represents several enhancements over the existing approach to realize MVCT to kVCT conversion [9] based on CycleGAN. In particular, our model resulted in a higher structure preservation and reduction in the training data.

To evaluate the image quality of the processed MVCT images, we performed visual, quantitative, and clinical evaluations. In the visual comparisons among the original MVCT, processed MVCT, and reference kVCT images, the processed MVCT images were noted to be significantly enhanced when even a small amount of training data of few ten slices was used. In particular, the noise was largely reduced, and the contrast between the soft tissues was enhanced while preserving the structures of the input image. The enhanced images can be used for accurate image registration of IGRT in helical tomotherapy. Furthermore, a quantitative enhancement in several indexes, including the HU values of soft tissues, NSelf-SSIM, DIG, and CCE, was noted in terms of the image quality. When the training data size was increased, the values of the quantitative indexes became nearly constant for datasets ranging from a few hundreds of slices to thousand slices. In addition to the visual and quantitative evaluations, we conducted a clinical evaluation in which medical doctors contoured

the parotid glands in processed MVCT and original MVCT images, and we estimated the degree of coincidence of the contours by using the Dice coefficient. The Dice coefficient for the processed MVCT images was larger than that for the original MVCT images with a statistically significant difference. Furthermore, the clinical evaluation showed that the accuracy of contouring in the images processed using the model trained with data-256 was comparable to that using the model trained with data-full. The enhanced images and contours can be used to realize accurate ART and dose estimation at intermediate fractions, as the HU values are similar to those of kVCT, and the target and OAR are accurately contoured. Moreover, the proposed conversion model can be used not only for MVCT to kVCT conversion but also for several modality conversions relevant for RT. Future work will be aimed at overcoming the limitations associated with the metal artifacts and extending the applicability of the proposed model. This framework may facilitate dose calculation by using the processed MVCT images in the complete head and neck regions.

ACKNOWLEDGMENTS

Sho Ozaki was supported in part by a JSPS Grant-in-Aid for Scientific Research (C), 19K08093. Kanabu Nawa was supported in part by a JSPS Grant-in-Aid for Scientific Research (C), 20K08073. Toshikazu Imae was supported in part by a JSPS Grant-in-Aid for Scientific Research (C), 21K12121. Takahiro Nakamoto was supported in part by a JSPS Grant-in-Aid for Young Scientists, 18K15625. Akihiro Haga was supported in part by a JSPS Grant-in-Aid for Scientific Research (C), 19K08201. Keiichi Nakagawa was supported in part by a JSPS Grant-in-Aid for Scientific Research (B), 20H04278. We would like to thank Editage (www.editage.com) for English language editing.

-
- [1] Spadea MF, Maspero M, Zaffino P, Seco J. Deep learning-based synthetic-CT generation in radiotherapy and PET: a review. *arXiv preprint arXiv. 2021:2102.02734.*
 - [2] Wang T, Lei Y, Fu Y, et al. A review on medical imaging synthesis using deep learning and its clinical applications. *Journal of Applied Clinical Medical Physics. 2021;22(1):11-36.*
 - [3] Kaji S, Kida S. Overview of image-to-image translation by use of deep neural networks: denoising, super-resolution, modality conversion, and reconstruction in medical imaging. *Radi-*

- ological Physics and Technology. 2019;12(3):235-248.
- [4] Wolterink JM, Dinkla AM, Savenije MH, Seevinck PR, van den Berg CA, Išgum I. Deep MR to CT synthesis using unpaired data. In International workshop on simulation and synthesis in medical imaging 2017;14-23. Springer, Cham.
 - [5] Maspero M, Savenije MH, Dinkla AM, et al. Dose evaluation of fast synthetic-CT generation using a generative adversarial network for general pelvis MR-only radiotherapy. Physics in Medicine & Biology. 2018;63(18):185001.
 - [6] Kida S, Kaji S, Nawa K, et al. Visual enhancement of Cone-beam CT by use of CycleGAN. Medical Physics. 2020;47(3):998-1010.
 - [7] Liang X, Chen L, Nguyen D, et al. Generating synthesized computed tomography (CT) from cone-beam computed tomography (CBCT) using CycleGAN for adaptive radiation therapy. Physics in Medicine & Biology. 2019;64(12):125002.
 - [8] Taasti VT, Klages P, Parodi K, Muren LP. Developments in deep learning based corrections of cone beam computed tomography to enable dose calculations for adaptive radiotherapy. Physics and Imaging in Radiation Oncology. 2020;15:77-79.
 - [9] Vinas L, Scholey J, Descovich M, Kearney V, Sudhyadhom A. Improved contrast and noise of megavoltage computed tomography (MVCT) through cycle-consistent generative machine learning. Medical Physics. 2021;48(2):676-90.
 - [10] Goodfellow I, Pouget-Abadie J, Mirza M, et al. Generative adversarial nets. Advances in Neural Information Processing Systems. 2014;27.
 - [11] Westerly DC, Schefter TE, Kavanagh BD, et al. High-dose MVCT image guidance for stereotactic body radiation therapy. Medical Physics. 2012;39(8):4812-4819.
 - [12] Mackie TR, Holmes T, Swerdloff S, et al. Tomotherapy: a new concept for the delivery of dynamic conformal radiotherapy. Medical Physics. 1993;20(6):1709-19.
 - [13] Mackie TR. History of tomotherapy. Physics in Medicine & Biology. 2006;51(13):R427.
 - [14] Meeks SL, Harmon Jr JF, Langen KM, Willoughby TR, Wagner TH, Kupelian PA. Performance characterization of megavoltage computed tomography imaging on a helical tomotherapy unit. Medical Physics. 2005;32(8):2673-2681.
 - [15] Ruchala KJ, Olivera GH, Schloesser EA, Mackie TR. Megavoltage CT on a tomotherapy system. Physics in Medicine & Biology. 1999;44(10):2597.

- [16] Ozaki S, Haga A, Chao E, et al. Fast statistical iterative reconstruction for mega-voltage computed tomography. *The Journal of Medical Investigation*. 2020;67(1.2):30-39.
- [17] Zhu JY, Park T, Isola P, Efros AA. Unpaired image-to-image translation using cycle-consistent adversarial networks. In *Proceedings of the IEEE international conference on computer vision* 2017;2223-2232).
- [18] Kikinis R, Pieper SD, Vosburgh KG. 3D Slicer: a platform for subject-specific image analysis, visualization, and clinical support. In *Intraoperative imaging and image-guided therapy*. Springer, New York, NY; 2014, pp. 277-289.
- [19] Chang YB, Xu D, Zamyatin AA. Metal artifact reduction algorithm for single energy and dual energy CT scans. In *2012 IEEE Nuclear Science Symposium and Medical Imaging Conference Record (NSS/MIC)* 2012; 3426-3429.
- [20] Teixeira PA, Meyer JB, Baumann C, et al. Total hip prosthesis CT with single-energy projection-based metallic artifact reduction: impact on the visualization of specific periprosthetic soft tissue structures. *Skeletal Radiology*. 2014;43(9):1237-1246.
- [21] Nakao M, Imanishi K, Ueda N, Imai Y, Kirita T, Matsuda T. Regularized three-dimensional generative adversarial nets for unsupervised metal artifact reduction in head and neck CT images. *IEEE Access*. 2020;8:109453-109465.
- [22] Lempitsky V, Vedaldi A, Ulyanov D. Deep image prior. In *2018 IEEE/CVF Conference on Computer Vision and Pattern Recognition* 2018;9446-9454.